Planetary bow shocks: Gasdynamic analytic approach

M. Verigin,[1,2] J. Slavin,[1] A. Szabo,[1] T. Gombosi,[3] G. Kotova,[4] O. Plochova,[4] K. Szegö,[5] M. Tátrallyay,[5] K. Kabin,[6] and F. Shugaev[7]

Received 30 September 2002; revised 9 January 2003; accepted 14 February 2003; published 16 August 2003.

[1] A new analytical model of the bow shock surface is suggested for reasonably accurate and fast prediction of this boundary's position near obstacles of different shape. For axially symmetric obstacles the model was verified by comparison with experiments and results of gasdynamic code application for a wide range of upstream polytropic indexes, $1.15 < \gamma < 2$, and Mach numbers, $1 < M_s < \infty$. The model can also be used for prediction of the bow shock position around nonaxially symmetric obstacles. *INDEX TERMS:* 2154 Interplanetary Physics: Planetary bow shocks; 3210 Mathematical Geophysics: Modeling; 2109 Interplanetary Physics: Discontinuities; 2149 Interplanetary Physics: MHD waves and turbulence; *KEYWORDS:* bow shocks, gasdynamic, analytic modeling, bow shock shape, magnetopause shape, boundary conditions

Citation: Verigin, M., J. Slavin, A. Szabo, T. Gombosi, G. Kotova, O. Plochova, K. Szegö, M. Tátrallyay, K. Kabin, and F. Shugaev, Planetary bow shocks: Gasdynamic analytic approach, *J. Geophys. Res.*, *108*(A8), 1323, doi:10.1029/2002JA009711, 2003.

1. Introduction

[2] The gasdynamic (GD) approximation still remains useful in studies of the planetary bow shocks and shock related phenomena. This approach works quite well when the MHD Mach numbers are high [*Spreiter and Stahara*, 1980; *Slavin and Holzer*, 1981; *Slavin et al.*, 1983], but it also provides a useful first approximation when the Alfvenic, M_a, or fast magnetosonic Mach, M_{ms}, numbers are low and these Mach numbers are substituted for the gasdynamic Mach number M_s [*Fairfield et al.*, 2001].

[3] Gasdynamic solutions can be used to set constraints on the polytropic index γ for different upstream conditions [*Farris et al.*, 1991] and in detailed analysis of the subsolar magnetosheath flow [*Song et al.*, 1999]. Furthermore, the gasdynamic convected field (GDCF) approximation to the full MHD treatment is also used widely [*Spreiter et al.*, 1966; *Spreiter and Stahara*, 1995].

[4] Though numerical GD codes [e.g., *Lyubimov and Rusanov*, 1970; *Spreiter and Stahara*, 1980] answer, in principle, all questions, these codes are quite complicated in use and are slowly converging for low Mach numbers ($M_s < 1.25$, *Lyubimov et al.* [1995]), while an exact theoretical solution is still available in the $M_s \rightarrow 1$ limit [e.g., *Shugaev*, 1965].

[5] On the other hand, theoretical considerations of the bow shock position and shape are quite controversial in modern space science literature (e.g., see GD theory review by *Fairfield et al.* [2001] and section 3 of this paper). They generally, for example, do not take into consideration the shape of the obstacle with the exception of the nose curvature radius, R_0 [*Farris and Russell*, 1994].

[6] In the present paper we will reevaluate the available theoretical GD expressions on the basis of a uniform presentation tied to the obstacle shape. Taking into account all basic approaches of theoretical GD analysis, new analytical expressions will be proposed for the standoff distance, nose curvature radius and shape of the GD shock as functions of γ, M_s, R_0, and the obstacle bluntness b_0.

[7] Our new expressions will be verified for different Mach numbers $1 < M_s < \infty$, polytropic indexes $1.15 < \gamma < 2$, and obstacle shapes ranging from disk, through blunt elliptic, spherical, elongated elliptic, parabolic, to hyperbolic. The possibility of scaling these expressions to describe the bow shock upstream of nonaxial symmetric obstacle will also be discussed.

2. Basic Relations

2.1. Obstacle Shape

[8] Throughout the paper we will use the following equation to describe the geometric properties of the obstacle:

$$y^2(x) = 2R_0(r_0 - x) + b_0(r_0 - x)^2. \quad (1)$$

It is the general expression for a conic section symmetric around the x axis. Conic sections can be expressed many other ways; however, equation (1) has the advantage that all its parameters r_0, R_0, and b_0 have clear geometrical interpretation: r_0 is the position of the obstacle nose, R_0 is

[1]NASA Goddard Space Flight Center, Greenbelt, Maryland, USA.
[2]Permanently at Space Research Institute, Russian Academy of Sciences, Moscow, Russia.
[3]Space Physics Research Laboratory, Department of Atmospheric, Oceanic and Space Sciences, University of Michigan, Ann Arbor, Michigan, USA.
[4]Space Research Institute, Russian Academy of Sciences, Moscow, Russia.
[5]KFKI Research Institute for Particle and Nuclear Physics, Budapest, Hungary.
[6]Department of Physics, University of Alberta, Edmonton, Alberta, Canada.
[7]Physical Faculty, Moscow State University, Moscow, Russia.

0148-0227/03/2002JA009711

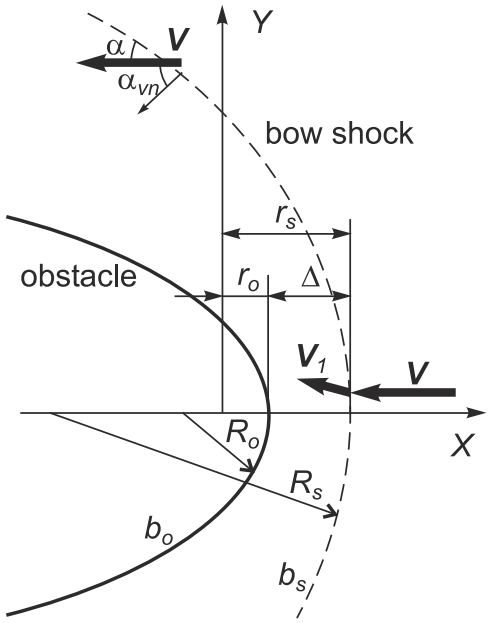

Figure 1. Definition of space variables: r_0 and r_s are distances to the obstacle and shock, respectively; R_0 and R_s are proper nose curvature radii; and b_0 and b_s stand for obstacle and shock bluntness, while Δ is the bow shock standoff distance.

its radius of curvature, and b_0 stands for the "bluntness" of the obstacle (Figure 1) with the nose part of the obstacle close to blunt elliptic for $b_0 < -1$, spherical for $b_0 = -1$, elongated elliptic for $-1 < b_0 < 0$, parabolic for $b_0 = 0$, and hyperbolic for $b_0 > 0$.

[9] A parameterization similar to equation (1) of the obstacle shape was used in accurate tables of gasdynamic flows by *Lyubimov and Rusanov* [1970]. In Appendix A, interrelations are presented between equation (1) and some of the other obstacle shape representations used either for empiric analysis of the observations or for setting up boundary conditions in theoretical calculations.

2.2. Fundamental Equations

[10] The fundamental differential equations of steady nondissipative perfect compressible gas flow [*Landau and Lifshitz*, 1959] are as follows:

$$\mathrm{div}(\rho \boldsymbol{V}) = 0 \tag{2a}$$

$$\rho(\boldsymbol{V}\nabla)\boldsymbol{V} = -\nabla p \tag{2b}$$

$$\mathrm{div}\left(\left(\frac{\rho \boldsymbol{V}^2}{2} + \frac{\gamma p}{\gamma - 1}\right)\boldsymbol{V}\right) = 0, \tag{2c}$$

where ρ, $\boldsymbol{V}$, p are the flow mass density, velocity, and pressure, respectively. The same equations are presented below in the form of GD parameter variation along the flow tube of cross section S:

$$(\rho V S)' = 0 \tag{3a}$$

$$\left(\rho V^2 S\right)' = -Sp' \tag{3b}$$

$$\left(VS\left(\frac{\rho V^2}{2} + \frac{\gamma p}{\gamma - 1}\right)\right)' = 0, \tag{3c}$$

where $'$ marks differentiation along the tube. The condition of adiabatic flow (equation (4a)) and the Bernoulli integral (equation (4b)) are straightforward consequences of relations (3a)–(3c).

$$\left(\frac{p}{\rho^\gamma}\right)' = 0 \tag{4a}$$

$$\left(\frac{V^2}{2} + \frac{\gamma}{\gamma - 1}\frac{p}{\rho}\right)' = 0 \tag{4b}$$

[11] Except for the Bernoulli integral, relations (2)–(4) describe continuous flows only. In the supersonic regime with $M_s = V/\sqrt{\gamma p/\rho} > 1$ the bow shock discontinuity is formed upstream of the obstacle (Figure 1). The following Rankine-Hugoniot relations are valid across this discontinuity [*Landau and Lifshitz*, 1959]:

$$[\rho V_n] = 0 \tag{5}$$

$$\left[\rho V_n^2 + p\right] = 0 \tag{6}$$

$$\left[\frac{V^2}{2} + \frac{\gamma}{\gamma - 1}\frac{p}{\rho}\right] = 0 \tag{7}$$

$$[\boldsymbol{V}_t] = 0, \tag{8}$$

where brackets define the difference between shock upstream and shock downstream bracketed expressions and where indexes n, t mark the normal and tangential velocity components. Relations (5)–(7) correspond well to equations (3a)–(3c), taking into account that $[S] = 0$ at the shock. Relation (8) just expresses the absence of tangential stresses at this discontinuity.

[12] It is convenient to express the solution of the Rankine-Hugoniot relations via parameters:

$$\varepsilon_\infty = \frac{(\gamma - 1)}{(\gamma + 1)}, \varepsilon = \varepsilon_\infty + \frac{2}{(\gamma + 1)M_s^2}, \varepsilon_n = \varepsilon + \frac{2\tan^2 \alpha_{vn}}{(\gamma + 1)M_s^2}, \tag{9}$$

where α_{vn} is the angle between $\boldsymbol{V}$ and the shock normal $\boldsymbol{n}$ (Figure 1). Then the GD variables behind the shock, marked by subscript 1, can be expressed as

$$\begin{aligned} &V_{1n} = \varepsilon_n V \cos\alpha_{vn}, V_{1t} = V \sin\alpha_{vn}, \quad \rho_1 = \rho/\varepsilon_n \\ &p_1 = p\frac{(\gamma + 1) - \varepsilon_n(\gamma - 1)}{(\gamma + 1)\varepsilon_n - (\gamma - 1)}. \end{aligned} \tag{10}$$

The third equation of relation (10) gives a physical sense to parameter ε_n: it is the reciprocal gas density compression ratio $(\rho_1/\rho)^{-1}$ across the shock. Then ε becomes the reciprocal of the largest compression ratio across the shock, which is achieved at its nose point where $\alpha_{vn} = 0$ (Figure 1),

and ε_∞ is the reciprocal of the maximal possible compression ratio, which is achieved when $\alpha_{vn} = 0$ and $M_s \to \infty$.

[13] Far downstream of the obstacle, the bow shock becomes very weak and $\varepsilon_n \to 1$. Then from equation (9) it follows:

$$\tan^2 \alpha_{vn}\big|_{\varepsilon_n \to 1} = (1-\varepsilon)(\gamma+1)M_s^2/2 = M_s^2 - 1,$$
$$\text{i.e., } \cos \alpha_{vn}\big|_{\varepsilon_n \to 1} = \sin \alpha = 1/M_s. \tag{11}$$

The last equality in equation (11) is the well-known relation for the asymptotic slope α (Figure 1) of the Mach cone [e.g., see *Spreiter and Stahara*, 1985].

2.3. Curved Shock Boundary Condition

[14] The application of relations (10) to calculate the velocity $\boldsymbol{V}_1$ at a small distance y from the x axis (see Figure 1) leads to

$$\boldsymbol{V}_1 = \left(V_{1x}, V_{1y}\right) \approx V(-\varepsilon, y(1-\varepsilon)/R_s). \tag{12}$$

Only linear terms of y were kept in equation (12). During time dt after passing of the shock, a parcel of gas will be displaced by $dx = V_{1x}dt = -\varepsilon V dt$ and $dy = V_{1y}dt = y(1-\varepsilon)Vdt/R_s$ along and perpendicular to the x axis, respectively. It means that the axial flow tube cross section $S = \pi y^2$ will be increased by $dS = 2\pi y dy = 2\pi y^2(1-\varepsilon)Vdt/R_s$. Hence the relative rate of the flow tube expansion after the shock can be expressed as [e.g., see *Biermann et al.*, 1967; *Wallis*, 1973]:

$$\frac{1}{S}\frac{dS}{dx} = -\frac{2}{R_s}\cdot\frac{1-\varepsilon}{\varepsilon}. \tag{13}$$

[15] Boundary condition (13) includes the nose radius of curvature R_s and is applicable for curved shocks only. With the aid of equation (3a) this boundary condition can be rewritten as

$$\frac{(\rho V)'}{\rho V} = \frac{2}{R_s}\cdot\frac{1-\varepsilon}{\varepsilon} \approx \frac{V'}{V} \approx \frac{1}{\Delta}. \tag{14}$$

The second approximate equality in equation (14) was written taking into account that the gas flow is subsonic behind the shock nose and hence approximately incompressible $\rho \approx$ const. The third approximate equality is valid only when the bow shock stand of distance Δ (Figure 1) is small (e.g., in the hypersonic limit with $M_s \to \infty$, $\gamma \to 1$). Then the Δ/R_s ratio becomes a function of only the reciprocal relative compression ratio ε^*:

$$\varepsilon^* = \frac{\varepsilon}{1-\varepsilon} = \frac{(\gamma-1)M_s^2+2}{2\left(M_s^2-1\right)} = \left.\frac{\rho}{\rho_1-\rho}\right|_{\alpha_{vn}=0}. \tag{15}$$

3. Empiric GD Relations and Approaches Used for Bow Shock Parameterization

3.1. Standoff Distance

[16] Almost all of the approximate relations for the standoff distance of the bow shock Δ (Figure 1) are based on the empirical conclusion that both Δ and R_s are mainly functions of ε (equation (9)) or, equivalently, ε^* (equation (15)), at least when M_s is sufficiently high. To some extent, this conclusion is supported by GD experiments, observations of flow about the planets [*Slavin et al.*, 1983], and calculations. The first relations for Δ were generated by *Serbin* [1958], *Ambrosio and Wortman* [1962], and *Seiff* [1962] for the flow around a sphere ($b_0 = -1$, see equation (1)). These are

$$\Delta = \frac{2}{3}R_0\varepsilon^*, \Delta = 0.52R_0\varepsilon^*, \text{and } \Delta = 0.78R_0\varepsilon, \tag{16}$$

respectively. Note that in the first two relations $\Delta \to \infty$ when $M_s \to 1$ according to equation (15). This behavior is qualitatively reasonable, though the correct rate of Δ approaching to infinity should be different as was deduced by equation (17) [*Hida*, 1955; *Shugaev*, 1964]:

$$\Delta \sim (M_s - 1)^{-2/3} \sim \varepsilon^{*2/3}. \tag{17}$$

[17] In space science papers the empiric relation by *Spreiter et al.* [1966] is used most frequently, which is based on the approach of *Seiff* [1962] but which is applicable for flows around a body with bluntness $b_0 = -(19 + \sqrt{21})/30 \approx -0.786$ (see line 7 in Table A1 of Appendix A). Taking into account that in the GD calculations of *Spreiter et al.* [1966] the obstacle nose radius of curvature was not equal to one (line 7 in Table A1), their relation can be rewritten as

$$\Delta = 1.1\frac{\sqrt{21}-3}{2}R_0\varepsilon = 0.87R_0\varepsilon, \qquad 5 < M_s < \infty. \tag{18}$$

The greater distance between the obstacle and the shock in relation (18), compared with those in the last of relation (16), is the result of the greater bluntness of *Spreiter et al.*'s [1966] obstacle compared with the bluntness of a sphere.

[18] *Farris and Russell* [1994] noted that in relation (18) of *Spreiter et al.* [1966] Δ is not approaching infinity when $M_s \to 1$, and intuitively modified the formula:

$$\Delta = 0.87R_0\frac{\varepsilon M_s^2}{M_s^2-1}. \tag{19}$$

However, the rate of Δ approaching infinity when $M_s \to 1$ remained incorrect (cf. relation (17)). *Farris and Russell* [1994] also assumed that Spreiter's obstacle had a nose radius of curvature $R_0 = 1.35\ r_0$, while, in fact, it was $R_0 = r_0\left(3+\sqrt{21}\right)/6$ (line 7 in Table A1). It was corrected in expression (19).

[19] The correct power of Δ approaching infinity when $M_s \to 1$ was implemented in an empiric relation by *Verigin et al.* [1997a, 1999]:

$$\Delta = R_0\left(\varepsilon^*/\left(1.87 + 0.86/\varepsilon^{*3/5}\right)\right)^{2/3}. \tag{20}$$

This expression approximated well the standoff distance of the bow shock calculated by *Spreiter and Stahara* [1995] with the use of GD codes for $M_s > 1.15$ ($b_0 \approx 0.786$), while relations (18), (19) underestimated or overestimated Δ for

small Mach numbers, respectively [*Verigin et al.*, 1997a, 1999].

[20] *Minailos* [1973] proposed some other empiric relations for Δ. Specific to his parameterization is the use of

$$\hat{\varepsilon} = \varepsilon + \frac{0.07}{M_s^2} = \varepsilon + 0.07\frac{\gamma+1}{2}(\varepsilon - \varepsilon_\infty) \tag{21}$$

instead of ε in the approximating relations. For a flow around a sphere *Minailos* [1973] arrived at

$$\Delta = R_0\,\hat{\varepsilon}\left(0.76 + 1.05\,\hat{\varepsilon}^2\right). \tag{22}$$

Relation (22) approximates well the bow shock standoff distance for $\hat{\varepsilon} < 0.4$ or $M_s{}^2 > (2 + 0.07(\gamma+1))/(1.4 - 0.6\gamma)$, taking into account equation (21). For a flow around an ellipsoid ($-\infty < b_0 < -0.25$) *Minailos* [1973] introduced a relation that can be rewritten in our notations as

$$\Delta = \frac{R_0}{\sqrt{-b_0}}\,\hat{\varepsilon}\left(1.584 - \frac{0.982}{\sqrt{-b_0}} - \frac{0.18}{b_0} + 1.05\,\hat{\varepsilon}^2\right) + \frac{R_0}{\sqrt{-b_0}} \cdot \begin{cases} 0.17 - 0.38/\sqrt{-b_0} - 0.29/b_0, & -\infty < b_0 < -2.78, \\ 0, & -2.78 < b_0 < -0.25. \end{cases} \tag{23}$$

Probably only this relation reproduces analytically the standoff distance for flows around bodies of different shape. Unfortunately, it may contain misprints: the round bracketed expression in equation (23) for flows around a sphere ($b_0 = -1$) is slightly different from the similar expression in equation (22); the upper level relation after the figure bracket in equation (23) would better correspond to the curve plotted in *Minailos*'s [1973] Figure 1 for $b_0 = -4$ (ratio of flow parallel to the perpendicular ellipsoid axes is equal to 0.5) whether it is multiplied by $\hat{\varepsilon}$.

[21] Empirical relations for the bow shock standoff distance Δ, relevant to the flow around a "dipole" pressure balanced boundary (Table A1 of Appendix A, line 7), are compared in Figure 2. Solid squares in Figure 2 are the results of the GD calculations of *Spreiter and Stahara* [1995] extended to M_s values smaller than in the original *Spreiter et al.* [1966] paper. Empirical relation (18) [*Spreiter et al.*, 1966] underestimates Δ, while relation (19) [*Farris and Russell*, 1994] overestimates Δ for small M_s. Relation (23) by *Minailos* [1973] has a longer range of approximate applicability, but it still incorrectly restricts the standoff distance when $M_s \to 1$.

3.2. Nose Radius of Curvature

[22] On the basis of the constant density approximation *Hayes and Probstein* [1966] derived a relation between the bow shock nose radius of curvature R_s and the standoff distance:

$$R_s = \frac{\Delta}{\varepsilon}\left(1 + \sqrt{\frac{8\varepsilon}{3}}\right), \tag{24}$$

which turned out to be "empirically valid over a wide range of ε." *Stulov* [1969] assumed that equation (24) should be a universal function of ε for all bodies and compared this

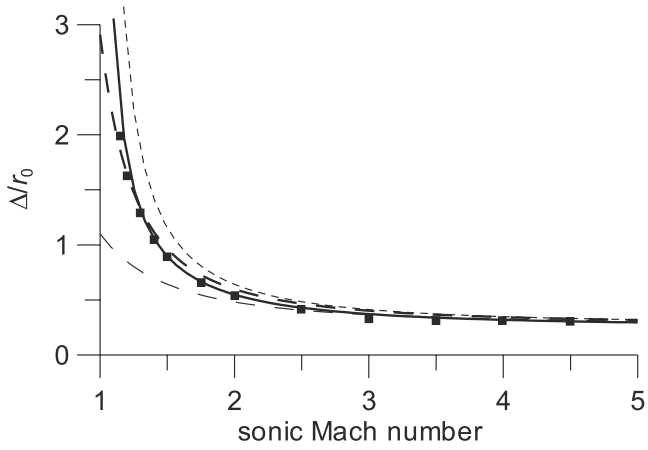

Figure 2. Comparison of the GD simulation results (filled squares) with empirical relations (18), long, thin dashes; (19), short, thin dashes; and (23), long, thick dashes, calculated for, $R_0 = r_0(3 + \sqrt{21})/6$, $b_0 = -(19 + \sqrt{21})/30$, and $\gamma = 5/3$. Smooth line is the empirical relation (35) suggested in section 4.2.

expression with the results of GD experiments with ellipsoids ($-9 < b_0 < -0.25$), finding that at small Mach numbers ($M_s \le 3$) the Δ/R_s ratio becomes dependent on the body bluntness too.

[23] A deficiency of relation (24) for small Mach numbers is also revealed from theoretical consideration by *Shugaev* [1965]. According to his analytical solution the bow shock shape in the vicinity of the x axis can be expressed as

$$x|_{M_s\to 1} = \frac{1.229c}{2}\left(\frac{\rho_c V_c}{\rho V} - 1\right)^{-1/3} - \frac{4}{3c}\sqrt{\frac{\gamma+1}{2}}\left(\frac{\rho_c V_c}{\rho V} - 1\right)^{5/6} y^2 + \ldots, \tag{25}$$

where c = const, ρ_c and V_c are, respectively, the flow density and velocity at the critical point where $V_c^2 = \gamma p_c/\rho_c$. Substitution of the last relation into the Bernoulli integral (equation (4b)) provides the possibility to evaluate $V_c = \sqrt{\varepsilon}V$ and $\gamma p_c/\rho_c = \varepsilon V^2$. The latter relation, together with the adiabatic flow relation (equation (4a)) $p_c/\rho_c^\gamma = p_1/\rho_1^\gamma$ and Rankine-Hugoniot conditions (equation (10)), provides the possibility to evaluate ρ_c and, finally,

$$\rho_c V_c = \frac{\rho V}{\sqrt{\varepsilon}}\left(\frac{2}{\gamma + 1 - \varepsilon(\gamma-1)}\right)^{1/(\gamma-1)}$$

and

$$\left(\frac{\rho_c V_c}{\rho V} - 1\right)\Big|_{M_s\to 1} \to \frac{\gamma+1}{8}(1-\varepsilon)^2\Big|_{\varepsilon\to 1} \to \frac{\gamma+1}{8\varepsilon^{*2}}\Big|_{\varepsilon^*\to\infty}. \tag{26}$$

Relation (26) together with expression (25) leads to the correct asymptotic relations for the standoff distance and nose radius of curvature of a GD bow shock:

$$\Delta|_{\varepsilon^*\to\infty} = \frac{1.229c}{(\gamma+1)^{1/3}}\varepsilon^{*2/3} \tag{27}$$

$$R_s|_{\varepsilon^*\to\infty} = \frac{3c}{(\gamma+1)^{4/3}}\varepsilon^{*5/3}. \tag{28}$$

From relations (27), (28) it follows that radius of curvature of the nose of the bow shock increases much faster than the standoff distance when $M_s \to 1$ ($\varepsilon \to 1$, $\varepsilon^* \to \infty$), that is, $R_s/\Delta \to \infty$ and does not remain constant as follows from relation (24).

[24] The correct power of R_s approaching infinity when $M_s \to 1$ is in the empiric relation given by *Verigin et al.* [1997a, 1999]:

$$R_s = R_0[(1.058 + \varepsilon^*)/1.067]^{5/3}, \tag{29}$$

which also agrees with expression (24) when $M_s \to \infty$ [*Verigin et al.*, 1999].

3.3. Shape of the Shock

[25] It is generally recognized [e.g., see *Van Dyke*, 1958] that the nose part of the bow shock formed by a wide class of obstacles can be approximated by a conic section:

$$y^2(x) = 2R_s(r_s - x) + b_s(r_s - x)^2, \tag{30}$$

where $r_s = r_0 + \Delta$ (Figure 1). Properties of the parameters Δ and R_s were discussed in sections 3.1 and 3.2.

[26] In order to analyze the behavior of the shock bluntness b_s, *Maslennikov* [1967] transformed the x, y coordinates of the bow shock cross section observed in his experiment into the $\left(\frac{y^2}{2(r_s-x)}, (r_s - x)\right)$ plane. In this coordinate system all shocks ($1.4 < M_s < 11.5$), formed around a hemispherical obstacle in Argon ($\gamma = 5/3$), air ($\gamma = 7/5$), and Freon 14 ($\gamma \approx 1.15$), become straight lines and thus are in agreement that their nose parts are really conic sections (equation (30)). Twice the tangent of the slope of these straight lines provides the possibility to determine the bluntness of individual shocks.

[27] It turns out that the bluntness of the shock, b_s, is a function of M_s mainly [*Maslennikov*, 1967], but not of ε, as in the cases of Δ and R_s. In all gases, b_s changed its sign from positive to negative around $M_s = 2$–2.5, that is, the nose part of the bow shock changed its shape from hyperbolic, through parabolic, into elliptic with increasing M_s. On the other hand, all studied cases were supersonic with the asymptotic slope of Mach cones expected to be $\sin\alpha = 1/M_s$ (equation (11)). These are the only hyperbolic curves among conic sections that can have such properties. The conclusion from this apparent contradiction is that bow shocks cannot be approximated by a simple conic section from its nose to far downstream, and a more sophisticated approach is required.

[28] To solve the above controversy, *Verigin et al.* [1999] proposed to describe the bow shock shape with the following expression:

$$x = r_0 + \Delta + \chi R_s\left(M_s^2 - 1\right) - \frac{1}{2}(1-\chi)y\sqrt{\left(M_s^2 - 1\right)} - \chi R_s\left(M_s^2 - 1\right)\sqrt{1 - \frac{(1-\chi)y}{\chi R_s\sqrt{M_s^2 - 1}} + \frac{(1+\chi)^2 y^2}{4\chi^2 R_s^2\left(M_s^2 - 1\right)}}. \tag{31}$$

This curve has a theoretically justified asymptotic downstream slope (equation (11)), the same standoff distance and nose radius of curvature as the conic section (equation (30)), but still has the possibility to adjust the bluntness of GD shocks by fitting a "shape parameter" χ. With the use of $\chi = 0.38R_0/r_0 - 0.47 + 3.63/\gamma^2 - 0.35/\varepsilon^*$ [*Verigin et al.*, 1999] or, later, $\chi = 3.2/(M_s + 1)$ [*Verigin et al.*, 2001a, 2001b], a reasonable correspondence of shocks calculated by GD codes [*Spreiter et al.*, 1970; *Spreiter and Stahara*, 1995] and approximated by equation (31) was achieved [e.g., see *Verigin et al.*, 1999, Figure 3]. This correspondence was approximately valid for $M_s = 2$, 4, 8, $\gamma = 5/3$, 2, and $0.01 < H/r_0 < 1$ ($-0.98 < b_0 < -0.4$ in accordance with line 8 of Table A1 of Appendix A) though the b_0 parameter was not used then.

[29] Summarizing section 3, we may conclude that the available analytic approaches to describe GD bow shock properties do not provide the possibility of rapid prediction of its position and shape for a wide range of upstream γ and Mach numbers for obstacles of different bluntness b_0. An attempt to provide a consistent analytic description of GD bow shock shape and position upstream of different obstacles will be the topic of section 4.

4. Bow Shock Modeling Approach

4.1. Shock Shape and Main Arguments of its Parameters

[30] Instead of the quite complicated relation (31) for the bow shock shape, we will use the following rational function of $(r_0 + \Delta - x)$:

$$y^2(x) = 2R_s(r_0 + \Delta - x) + \frac{(r_0 + \Delta - x)^2}{M_s^2 - 1} \cdot \left(1 + \frac{b_s\left(M_s^2 - 1\right) - 1}{1 + d_s(r_0 + \Delta - x)/R_s}\right). \tag{32}$$

Relation (32) corresponds exactly to conic section (equation (30)) for $d_s = 0$ and provides the correct asymptotic downstream slope (equation 11) for any $d_s > 0$, while the experimentally justified shape (equation (30)) is still valid in the vicinity of bow shock nose point $x = r_0 + \Delta$. Next, the additional inequality

$$b_s > \frac{\sqrt{2d_s\left(M_s^2 - 1\right) + 1}}{M_s^2 - 1}\left(2 - \sqrt{2d_s\left(M_s^2 - 1\right) + 1}\right) \tag{33}$$

leaves only convex surfaces among those described by relation (32).

[31] The quality of shock description by expression (32) with constraint (equation (33)) was checked by individual fitting of R_s, b_s, and d_s (Δ was fixed by the position of the nose point) to each of the 35 shocks tabulated by *Lyubimov and Rusanov* [1970] (Table 1). The specific standard deviation of the tabulated shock points from surfaces (equation (32)) is as small as $\sim 6 \times 10^{-4} R_0$. It is the accuracy of the shock tables by *Lyubimov and Rusanov* [1970] (three valid digits to the right of the decimal point) that allows the possibility of a reasonably accurate determination of the three above parameters of the smooth curve (equation (32)). Thus we used these tables for acquiring the basic dependencies of Δ, R_s, b_s, d_s on M_s and b_0 for $\gamma = 7/5$, while other entries of the Table 1 were used for the expansion of the basic depen-

Table 1. List of Polytropic Indexes, Obstacle Bluntnesses, and Sonic Mach Numbers Used for the Bow Shock Modeling

Reference	γ	b_0	M_s
Lyubimov and Rusanov [1970]	7/5	−1	1.5, 2, 3, 4, 5, 6, 7, 8, 10, 20, ∞
		−0.25	2, 4, 6, 20, ∞
		0	2, 4, 6, 8, 10, 20, ∞
		0.031	2, 4, 6, 20, ∞
		0.217	2, 4, 6, 20, ∞
		0.490	4, 6
Spreiter and Stahara [1995]	5/3	−0.786	2, 4, 8
	2		2, 4, 8
Spreiter et al. [1970]	5/3	−0.981, −0.878, −0.777, −0.644, −0.520, −0.400	8
Stahara et al. [1989]	2	−0.51	10, 12
Maslennikov [1967]	1.15	−∞	1.67, 2.3, 3.24, 3.8, 6.14,7.43, 9.17
	7/5		1.84, 2.03, 2.91, 3.98, 4.35,5.92
	5/3		1.54, 1.95, 2.47, 2.78, 3.63,5.1, 5.65
	1.15	−1	2.03, 3.06, 3.43, 4.0, 5.1, 8.9,11.8
	7/5		1.5, 2.09, 3.28, 4.2, 6.15
	5/3		1.4, 2.12, 2.84, 4.1, 6.0

dencies into $1.15 < \gamma < 2$ region and for the verification of the obtained results.

[32] Parameters of equation (32) are listed in order of their influence on the shape of the bow shock starting from the nose, and are defined as follows: (1) Δ, standoff distance, determines the nose position itself; (2) R_s, radius of curvature, determines the shock shape close to the nose; (3) b_s, bluntness, determines the shock shape further from the nose than R_s; (4) d_s provides the transition from the bluntness influenced region to the asymptotic regime; and (5) M_s determines the asymptotic bow shock slope.

[33] In accordance with the review in sections 3.1 and 3.2, parameters Δ and R_s should be functions of ε, ε^* mainly. Taking into account *Minailos*'s [1973] approach (equation (21)) and the asymptotic relations (equations (27) and (28)), we will search for expressions of these parameters as functions of

$$\hat{\varepsilon}^* = \varepsilon^* + \mathrm{const}(\gamma+1)(\varepsilon^* - \varepsilon_\infty{}^*), \tag{34}$$

where $\varepsilon^*_\infty = (\gamma - 1)/2$ is the value of the reciprocal relative compression ratio ε^* (equation (15)) when $M_s \to \infty$, and const = 1/50 according to the results of the following section. Next in the list of parameters, b_s will be investigated as a function of M_s only (see *Maslennikov* [1967] and section 3.3). We would expect a similar behavior from d_s parameter, which controls the shock shape between the zone of b_s influence and asymptotic region.

4.2. Functional Presentation of the Bow Shock Parameters

[34] Expressions (35)–(37) are the resulting dependencies of Δ and R_s on $\bar{\varepsilon}$, and b_s on M_s, respectively:

$$\Delta\left(\hat{\varepsilon}^*, R_0\right) = \frac{1.229c(b_0)\varepsilon^{*2/3}R_0}{(\gamma+1)^{1/3}(1+(\gamma+1)/50)^{2/3}}\left(1 - \frac{b(b_0,\gamma)}{\bar{\varepsilon}^{*1/6}}\right), \tag{35}$$

$$R_s\left(\hat{\varepsilon}^*, R_0\right) = 3c(b_0)\,\hat{\varepsilon}^{*5/3}R_0 \cdot\left(\frac{1}{(\gamma+1)^{4/3}(1+(\gamma+1)/50)^{5/3}} - \frac{a(b_0,\gamma)}{\hat{\varepsilon}^{*d(b_0)}}\right), \tag{36}$$

$$b_s(M_s) = \frac{1}{M_s^2-1} + e(b_0,\gamma) + \frac{21e^2(b_0,\gamma)/17 - 14e(b_0,\gamma)/9 + 7/4}{1 - 23e(b_0,\gamma)/30}\cdot\frac{M_s^2+1}{M_s^4}, \tag{37}$$

$$d_s(b_0) = \exp\left(\frac{107}{29} - \frac{371}{68}\left(\frac{8(b_0-4/21)}{13} + \left(1 + \left|\frac{8(b_0-4/21)}{13}\right|^{11/7}\right)^{7/11}\right)\right). \tag{38}$$

Despite the high accuracy of the *Lyubimov and Rusanov* [1970] tables, it turns out to be impossible to obtain a stable evaluation of d_s dependence on M_s perhaps because of insufficient inclusion in the tables of the downstream part of the shocks. So, expression (38) presents the dependence of d_s parameter just on the obstacle bluntness b_0. For the other shock parameters dependencies on b_0 are contained in the a, b, c, d, and e coefficients described by relations (39)–(43), respectively:

$$a(b_0,\gamma) = \frac{1}{2}\left(\frac{52}{25} + \frac{97}{84} - \frac{33}{10}\left(\frac{1}{(\gamma+1)^{13/4}} - \frac{1}{(12/5)^{13/4}}\right)\right)\cdot\left(1 - \frac{7b_0/16}{\left(1+|7b_0/16|^{8/33}\right)^{33/8}}\right) + \frac{33}{10}\left(\frac{1}{(\gamma+1)^{13/4}} - \frac{1}{(12/5)^{13/4}}\right) - \frac{97}{84}, \tag{39}$$

$$b(b_0,\gamma) = \frac{1}{2}\left(-\frac{23}{35} + \frac{43}{3}\left(\frac{1}{(\gamma+1)^{68/13}} - \frac{1}{(12/5)^{68/13}}\right) - \frac{24}{13} + \frac{13}{18}\left(\frac{1}{\gamma^{57/13}} - \frac{1}{(7/5)^{57/13}}\right)\right)\cdot\left(1 - \frac{b_0 - 3/10}{\left(\sqrt{119/20} + \sqrt{|b_0 - 3/10|}\right)^2}\right) + \frac{24}{13} - \frac{13}{18}\left(\frac{1}{\gamma^{57/13}} - \frac{1}{(7/5)^{57/13}}\right), \tag{40}$$

$$c(b_0) = \frac{6}{5}\left(17b_0/20 + \left(1 + |17b_0/20|^{5/3}\right)^{3/5}\right) + \frac{41/52}{\sqrt[4]{(26/9)^2 + b_0^2}}, \tag{41}$$

$$d(b_0) = \frac{1}{2}\left(\frac{85}{47} - \frac{15}{29}\right) \cdot \left(1 - \frac{19(b_0 - 39/70)/33}{\left(1 + |19(b_0 - 39/70)/33|^{5/6}\right)^{6/5}}\right) + \frac{15}{29}, \quad (42)$$

$$e(b_0, \gamma) = \left(1 - \frac{b_0 + 841/61 + 160\left(\gamma^{-16/5} - (7/5)^{-16/5}\right)/11}{\sqrt{(809/18)^2 + \left(b_0 + 841/61 + 160\left(\gamma^{-16/5} - (7/5)^{-16/5}\right)/11\right)^2}}\right) \cdot \frac{1}{2}\left(-\frac{1042}{17} - 40\left(\frac{1}{\gamma^{15/4}} - \frac{1}{(7/5)^{15/4}}\right) - \frac{1318}{39}\right) + \frac{1318}{39}. \quad (43)$$

[35] The explicit inclusion of power functions of γ into relations (35) and (36) provides the correct asymptotic behavior (equations (27) and (28)) for Δ and R_s when $\varepsilon^* \to \infty$ ($M_s \to 1$). The second term in equation (41) provides correct asymptotic behavior (equation (23)) of Δ when $b_0 \to -\infty$ (with $R_0/\sqrt{-b_0} = \text{const}$) and the obstacle is degraded to a disk of $R_0/\sqrt{-b_0}$ radius. All expressions (35)–(43) are monotonically increasing/decreasing, while expressions (38)–(40), (42), and (43) are also limited. All brackets containing γ become zero for $\gamma = 7/5$. In this case, the standard deviation of the shock points tabulated by *Lyubimov and Rusanov* [1970] from the bow shock model (equations (32) and (35)–(43)) is $\sim 8 \times 10^{-3} R_0$. The specific standard deviation of our bow shock model from the shock points scanned from figures of other authors given in Table 1 is $\sim 2 \times 10^{-2} R_0$.

[36] In Figure 2 we added the bow shock standoff distance (smooth line) calculated by our suggested relation (35) for a pressure-balanced case with a "dipole" magnetic field obstacle (Table A1, line7). Comparison of this curve with GD simulation results by *Spreiter and Stahara* [1995] demonstrates reasonably good mutual consistency over a wide range of M_s. It is worth noting again that our empiric relation has the correct asymptotic behavior when $M_s \to 1$, in contrast to the others shown in Figure 2.

4.3. Comparison With Results of GD Numerical Simulations and Experiments

[37] Figure 3 presents a comparison of the bow shock shapes from *Lyubimov and Rusanov* [1970] tables (points, $\gamma = 7/5$) with those calculated by relations (32) and (35)–(43) suggested in the present paper for flows around a sphere (a, $b_0 = -1$), ellipsoid (b, $b_0 = -0.25$), paraboloid (c, $b_0 = 0$), and hyperboloid (d, $b_0 = 0.217$). All points from the original tables were scaled and shifted along the x axis to achieve equal $r_0 = R_0 = 1$ for all obstacles, similar to the normalization proposed by *Verigin et al.* [2001a, 2001b] for the studies of planetary bow shocks. One additional shock with $M_s = 1.25$ was added to Figure 3a from the table by *Lyubimov et al.* [1995].

[38] The good agreement between our empiric relations and *Lyubimov and Rusanov*'s [1970] GD calculations is obvious. Taking into account that the correct asymptotic behavior (equations (27) and (28)) is implemented in our relations, we cannot be certain whether or not some of the difference between the modeled R_s and those corresponding to *Lyubimov et al.*'s [1995] table (Figure 3a, $M_s = 1.25$) is due to some insufficiency of our model. Another possible reason for some difference may be connected to the still incomplete convergence of GD numerical solutions for low Mach numbers, though *Lyubimov et al.* [1995] are certain of their solution for $M_s = 1.25$, but not for $M_s = 1.1$.

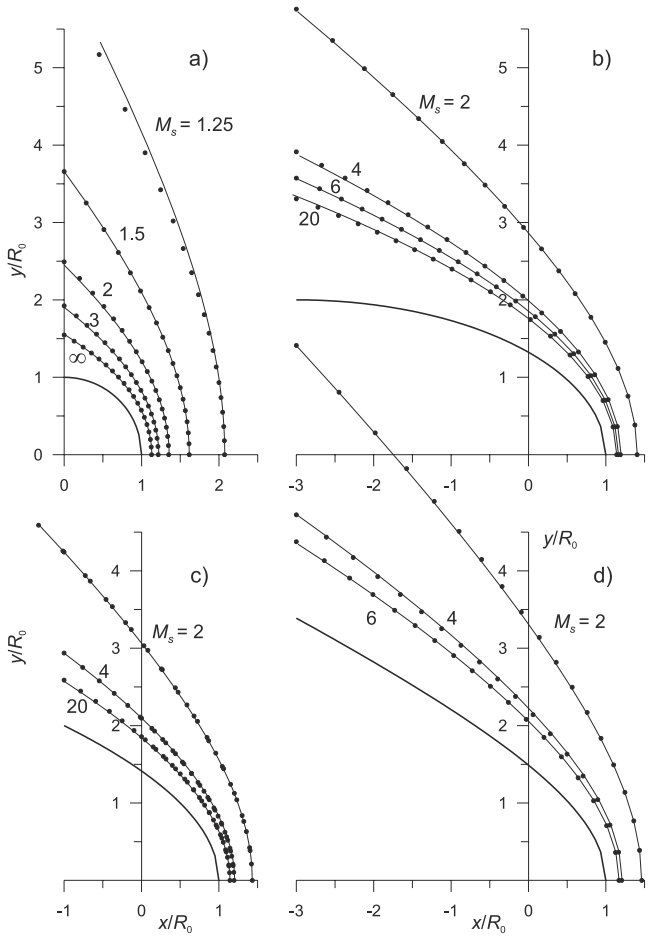

Figure 3. Comparison of the bow shocks calculated by GD code by *Lyubimov and Rusanov* [1970] (points) with those evaluated by relations (32) and (35)–(43) suggested in the present paper for flows around sphere (Figure 3a), ellipsoid (Figure 3b), paraboloid (Figure 3c), and hyperboloid (Figure 3d).

[39] Figure 4 displays the shock front formed by an end-on cylinder (top row) or hemisphere (bottom row) moving in Freon 14 (left column), air (middle column), and Ar (right column) scanned from the proper figures plotted by *Maslennikov* [1967] after his experiments. Smooth curves in the same figure are the shock surfaces according to relations (32) and (35)–(43) applied for flows around a disk (top row, $b_0 \to -\infty$ with $R_0/\sqrt{-b_0} = 1$ being the disk radius) and a sphere (bottom row, $b_0 = -1$). A reasonable correspondence of the experimental and modeled shocks in the range of $1.15 < \gamma < 5/3$ is obvious, though some disagreement observed in some case (e.g., for $b_0 = -1$, $M_s = 2.84$) is still present and is difficult to explain.

[40] Verification of our bow shock model by GD calculations for bigger values of $\gamma = 2$ is presented in the top row of Figure 5, while results for $\gamma = 5/3$ and obstacles of different shapes are displayed in the bottom row of Figure 5.

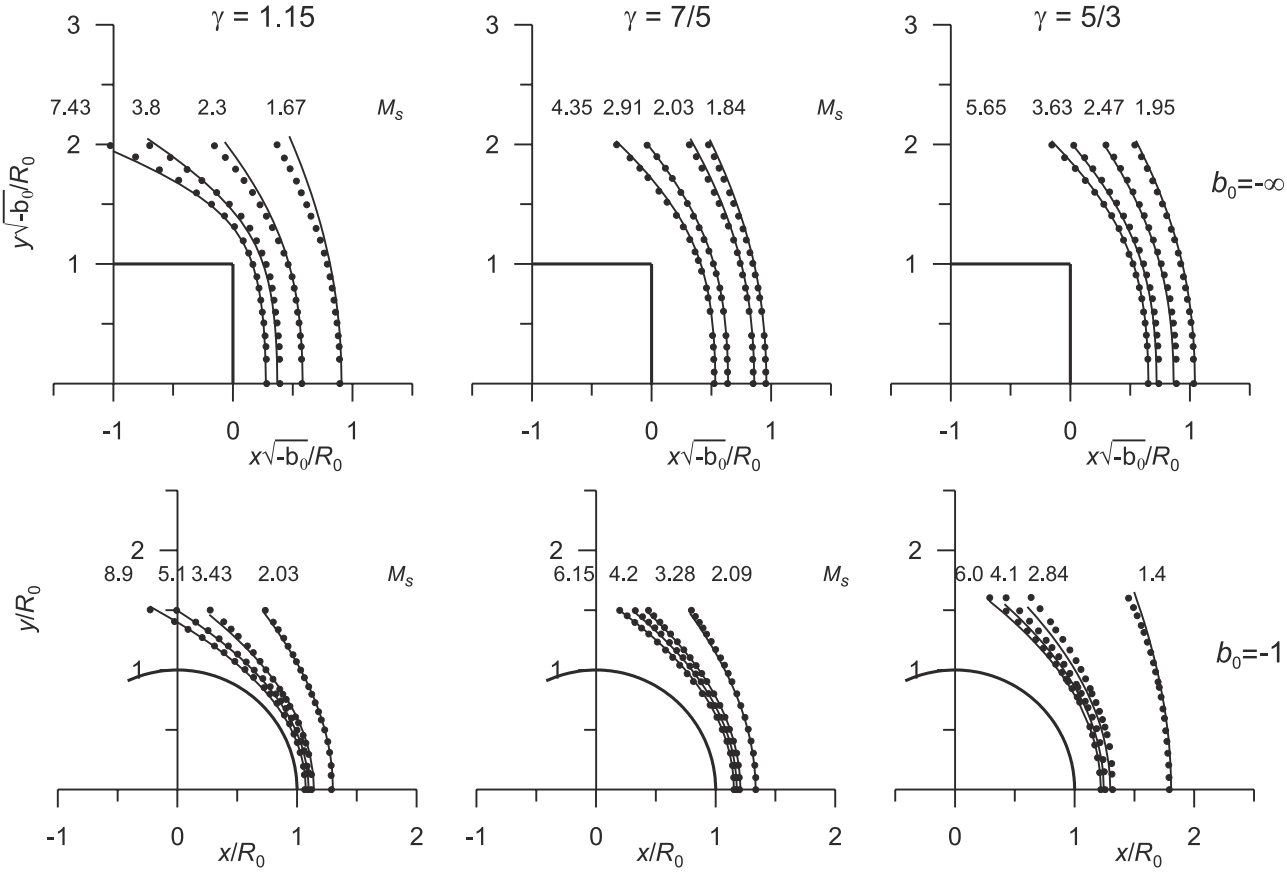

Figure 4. Comparison of the model bow shocks (smooth curves) by relations (32) and (35)–(43) with results of GD experiments (dots) by *Maslennikov* [1967].

The bow shock curve points in the left column of Figure 5 were scanned from the original Figure 12 by *Stahara et al.* [1989], where a flow around a "dipole" pressure balanced obstacle was considered (Table A1, line 7), that is, for obstacles specified by bluntness $b_0 \approx -0.786$. Bow shocks, formed by highly supersonic (M_s = 10, 12) flows around a blunter body with $b_0 \approx -0.51$ (see section 5 for more details) are scanned from the original Figures 9 and 10 by *Stahara et al.* [1989], and are given in the top right plot of Figure 5. Points in the bottom right corner of Figure 5 are taken from the original Figure 4 of *Spreiter et al.* [1970], where flows around bodies of different shapes formed by "ionospheric" pressure balanced obstacle were considered (Table A1, line 8). Variation of the H/r_0 parameter within the range $0.01 < H/r_0 < 1$ corresponds to obstacle bluntness variation within the range $-0.981 < b_0 < -0.4$. All points plotted in Figure 5 show reasonably good agreement with the smooth curves calculated by equations (32) and (35)–(43), thus confirming the applicability of our model. An opportunity to generalize the present bow shock model for the case of GD flows around a nonaxially symmetric obstacle will be considered in section 5.

5. Bow Shock Upstream of a Nonaxially Symmetric Body

5.1. Obstacle Shape and Standoff Distance Scaling

[41] Our approach to generalize for the case of a flow around nonaxially symmetric obstacles is based on the three-dimensional GD model by *Stahara et al.* [1989] developed for the analysis of the Jovian and Saturnian bow shocks. These planetary magnetospheres were shown by the Pioneer and Voyager observations to exhibit strong polar flattening and greatly reduced magnetosheath thicknesses [*Slavin et al.*, 1985]. Instead of an axially symmetric obstacle (equation (1)), *Stahara et al.* [1989] used a flattened obstacle, which can be well approximated by the following equation:

$$y^2 + \frac{R_{0y}}{R_{0z}} z^2 = 2R_{0y}(r_0 - x) + b_0(r_0 - x)^2, \qquad (44)$$

with $b_0 \approx 0.51$ and the two principal nose radii of curvature in the "equatorial" R_{0y} and "polar" R_{0z} planes. The cross section of an ellipsoid (equation (44)) by a plane x = const is an ellipse with an equatorial to polar axis ratio of $a/b = \sqrt{R_{0y}/R_{0z}}$. The equatorial magnetopause nose radii of curvature were fixed to $R_{0y} \approx 1.44\ r_0$ and $R_{0y} \approx 1.96\ r_0$ for Jupiter and Saturn, respectively. The polar magnetopause nose radii of curvature were variable and could be determined via the a/b flatness ratio that runs through a/b = 1, 1.5, 1.75, 2 for Jupiter and through a/b = 1, 1.15, 1.25, 1.35, 1,45 for Saturn with a/b = 1.75 (1.25) considered to be specific to Jupiter (Saturn).

[42] The R_{0y} and b_0 parameters of equation (44) were determined by fitting the surface (equation (44)) to the points scanned from the original Figures 6 and 8 of *Stahara et al.* [1989] at 10 cross sections of the obstacle by planes

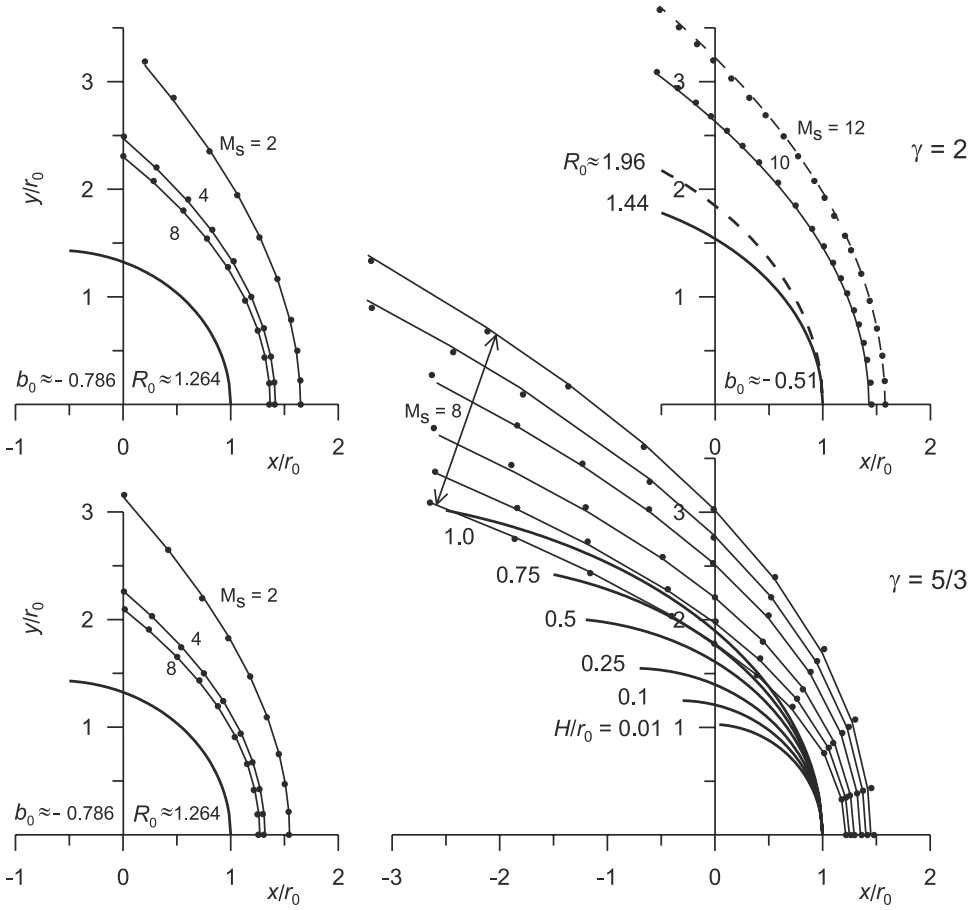

Figure 5. Comparison of the bow shocks calculated by GD codes (points) by *Spreiter et al.* [1970], *Stahara et al.* [1989], *Spreiter and Stahara* [1992] for obstacles of different shapes and $\gamma = 5/3, 2$ with model bow shocks (smooth curves) by relations (32) and (35)–(43).

with different clock angles $\varphi = \arctan(z/y)$ equidistantly spaced from 0° to 90°. The quality of the resultant obstacle fitting is shown in Figure 6 with the standard deviation of the obstacle surface from the scanned points of $\sim 2.5 \times 10^{-3} R_{0y}$. A specific feature of the obstacle (equation (44)) is that both the nose radius of curvature $R_{0\varphi}$ and the bluntness $b_{0\varphi}$ of its cross section by a plane φ = const are similar functions of φ:

$$R_{0\varphi} = \frac{R_{0y}}{\cos^2\varphi + R_{0y}\sin^2\varphi/R_{0z}} \tag{45}$$

$$b_{0\varphi} = \frac{b_0}{\cos^2\varphi + R_{0y}\sin^2\varphi/R_{0z}}. \tag{46}$$

It is natural and follows from the GD calculations by *Stahara et al.* [1989] that the standoff distance of the bow shock upstream of a nonaxially symmetric obstacle $\Delta(\bar{\varepsilon}^*, R_{0y}, R_{0z})$ should monotonically decrease with R_{0z} decreasing. Figure 7a presents the dependence on $a/b = \sqrt{R_{0y}/R_{0z}}$ of the bow shock standoff distances scanned from the original Figure 9 (points, M_s = 10) and Figure 10 (circles, M_s = 12) of *Stahara et al.* [1989] and normalized by the equatorial obstacle nose radius of curvature R_{0y}. The same points normalized by bow shock standoff distances in the case of a flow around an axially symmetric obstacle ($R_{0z} = R_{0y}$) are aligned along a simple proportional straight line with unit slope that independent of M_s (Figure 7b) when they are plotted as a function of the reciprocal $\sqrt{R_{0z}/R_{0y}}$ ratio. Thus we can assume that

$$\Delta\left(\hat{\varepsilon}^*, R_{0y}, R_{0z}\right) = \Delta\left(\hat{\varepsilon}^*, \sqrt{R_{0z}R_{0y}}\right), \tag{47}$$

with $\Delta\left(\bar{\varepsilon}^*, \sqrt{R_{0z}R_{0y}}\right)$ defined earlier by relation (35). According to relation (47) the standoff distance of the bow shock upstream of a nonaxially symmetric obstacle approaches, as expected, to that one for an axially symmetric obstacle when $R_{0z} \rightarrow R_{0y}$ and approaches to zero when $R_{0z} \rightarrow 0$ and the ellipsoid (equation (44)) degenerates to a zero thickness ellipse.

5.2. Radii of Curvature Scaling and Bow Shock Shape

[43] For the scaling of the bow shock nose radii of curvature it is reasonable to assume that the equatorial $R_{sy}(\bar{\varepsilon}^*, R_{0y}, R_{0z})$ and polar $R_{sz}(\bar{\varepsilon}^*, R_{0y}, R_{0z})$ bow shock nose radii of curvature coincide with those for an axially symmetric obstacle (equation (36)) when $R_{0z} = R_{0y}$. In the degenerate case, when $R_{0z} \rightarrow 0$, the equatorial shock radius should $R_{sy}(\bar{\varepsilon}^*, R_{0y}, R_{0z})$ approach R_{0y}. A more definite

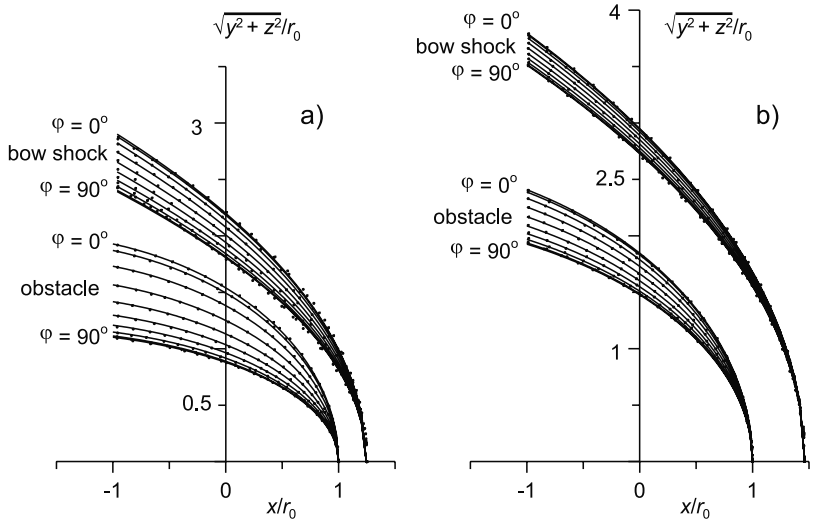

Figure 6. Comparison of the obstacles calculated by equation (44) for Jupiter (Figure 6a) with $\sqrt{R_{0y}/R_{0z}} = 1.75$ and for Saturn (Figure 6b) with $\sqrt{R_{0y}/R_{0z}} = 1.25$, and of the bow shocks calculated for these obstacles by relation (52) with obstacles used by *Stahara et al.* [1989] in their GD calculations and resultant shocks (points).

statement can be made of the behavior in the degenerate case of the polar shock nose radius of curvature , taking into account the nonaxially symmetric curved shock boundary condition deduced in Appendix B.

[44] From the boundary condition (B8), in a way used to deduce relation (14), we can conclude that

$$\left.\frac{1}{\Delta}\right|_{\Delta\to 0} \approx \frac{1}{\varepsilon^*}\left(\frac{1}{R_{sy}}+\frac{1}{R_{sz}}\right). \tag{48}$$

With the assumptions of the previous paragraph, relation (48) can be rewritten as

$$R_{sz}|_{\Delta\to 0} \approx \frac{\Delta}{\varepsilon^* - \Delta/R_{0y}} \approx \frac{\Delta}{\varepsilon^*}, \tag{49}$$

which defines the rate at which R_{sz} approaches zero as $R_{0z} \to 0$.

[45] All the limiting cases mentioned above are included in the following scaling relations:

$$R_{sy}(\bar{\varepsilon}^*, R_{0y}, R_{0z}) = R_s(\bar{\varepsilon}^*, R_{0y})\sqrt{\frac{R_{0z}}{R_{0y}}} + R_{0y}\left(1-\sqrt{\frac{R_{0z}}{R_{0y}}}\right)^{19/18} \tag{50}$$

$$R_{sz}(\bar{\varepsilon}^*, R_{0y}, R_{0z}) = \frac{\Delta(\bar{\varepsilon}^*, \sqrt{R_{0y}R_{0z}})}{\varepsilon^*}\left(1-\sqrt{\frac{R_{0z}}{R_{0y}}}\right)^2 + R_s(\bar{\varepsilon}^*, R_{0y})\left(\frac{R_{0z}}{R_{0y}}\right)^{11/18}, \tag{51}$$

with $\Delta\bar{\varepsilon}^*, \sqrt{R_{0z}R_{0y}})$ and $R_s(\bar{\varepsilon}^*, R_{0y})$ defined by relations (35) and (36), respectively; the powers of the both terms of both equations were selected on the basis of the best fit of the final bow shock model surface model to GD calculations by *Stahara et al.* [1989]. The final relation for the distance from the x axis to the bow shock upstream of a nonaxially symmetric body in the plane φ = const is quite similar to equation (32):

$$y^2+z^2 = 2R_{s\varphi}(r_0+\Delta-x) + \frac{(r_0+\Delta-x)^2}{M_s^2-1} \cdot \left(1+\frac{b_{s\varphi}(M_s^2-1)-1}{1+d_s(r_0+\Delta-x)/R_{s\varphi}}\right), \tag{52}$$

but now with

$$R_{s\varphi} = \frac{R_{sy}(\bar{\varepsilon}^*, R_{0y}, R_{0z})}{\cos^2\varphi + \sin^2\varphi R_{sy}(\bar{\varepsilon}^*, R_{0y}, R_{0z})/R_{sz}(\bar{\varepsilon}^*, R_{0y}, R_{0z})}, \tag{53}$$

$$b_{s\varphi} = \frac{b_s(M_s)}{\cos^2\varphi + \sin^2\varphi R_{sy}(\bar{\varepsilon}^*, R_{0y}, R_{0z})/R_{sz}(\bar{\varepsilon}^*, R_{0y}, R_{0z})}, \tag{54}$$

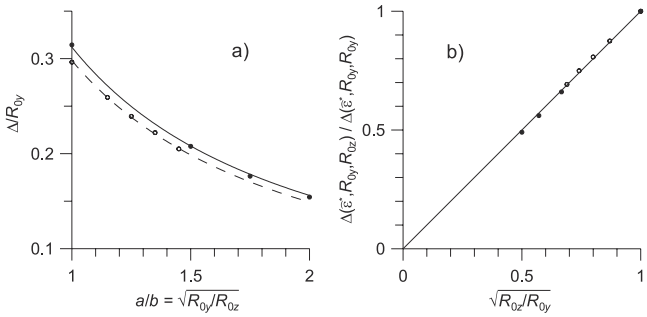

Figure 7. Dependence of the bow shock standoff distance in different normalizations (Figures 7a and 7b) on the ratio of the principal curvature radii of the obstacle nose. Proportional dependence with unit slope in Figure 7b implies simple generalization (equation (47)) of earlier deduced relation (35).

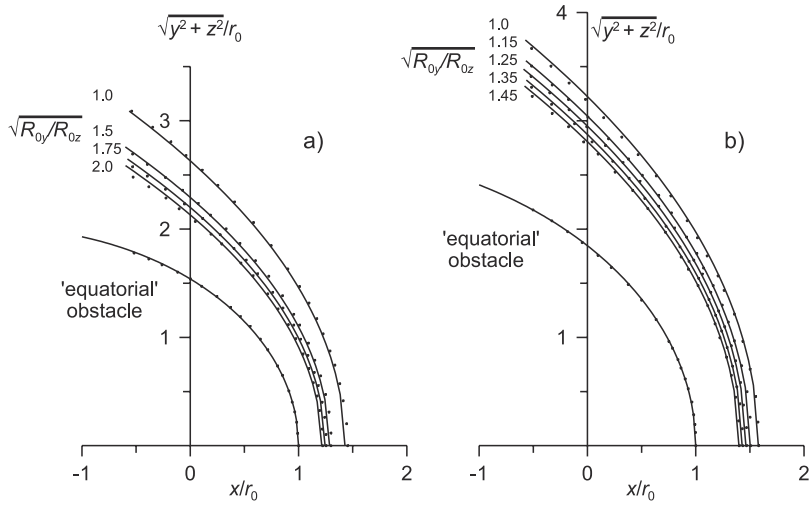

Figure 8. Comparison of the shocks evaluated by relation (52) with $\gamma = 2$ for obstacles with $R_{0y} = 1.44\, r_0$, $M_s = 10$ (Figure 8a) and $R_{0y} = 1.96\, r_0$, $M_s = 12$ (Figure 8b), and different R_{0y}/R_{0z} ratios with results of *Stahara et al.* [1989] GD simulations for similar obstacles (points).

and $\Delta(\bar{\varepsilon}^*, R_{0y}, R_{0z}), R_{sy}(\bar{\varepsilon}^*, R_{0y}, R_{0z}), R_{sz}(\bar{\varepsilon}^*, R_{0y}, R_{0z}), b_s(M_s), d_s(b_0)$ defined by relations (47), (50), (51), (37), and (38), respectively.

[46] Figure 8 presents the cross section by the equatorial plane ($z = 0$, $\varphi = 0$) of the 3-D bow shock surface (smooth lines) determined by relation (52) for different flatness ratios of the obstacle. Cross sections of the bow shock surface at two fixed R_{0y}/R_{0z} ratios by planes with different clock angles $0° \le \varphi \le 90°$ were presented in Figure 6. Reasonable correspondence of our model to the results of the GD calculations is evident in both figures. The standard deviation of the bow shock surface determined by relation (52) from the points scanned from the original figures is $\sim 7.5 \times 10^{-3} R_{0y}$.

6. Conclusions

[47] The analytical GD bow shock model described in the present paper provides the possibility of fast and reasonably accurate prediction of the position this boundary in front of obstacles of arbitrary bluntness b_0. For axially symmetric obstacles this model was verified by comparison with experiments and the results of GD numerical calculations over a wide range of upstream polytropic indices $1.15 < \gamma < 2$ and Mach numbers $1 < M_s < \infty$.

[48] The physical basis for the model parameters were discussed in detail and they offer the possibility that the model's validity is not limited to the nodes of the 3-D configuration space (M_s, γ, b_0), for which it was verified in the section 4.3, but also in the space between and outside of the range of these nodes. Moreover, this supposition is sustained by the theoretically correct asymptotic downstream slope of the modeled bow shock surface and by its correct asymptotic dependence on M_s and γ in the $M_s \to 1$ limit.

[49] Of course, many aspects of our model are empirically, experimentally, and computationally based. From the formal point of view it means that some caution should be exercised in the application of this model beyond the verified cases. Special precautions should be exercised while using the results of section 5 because they are based on the results of GD modeling with $M_s = 10$, 12 and $b_0 = -0.51$ only and for obstacles with fixed relation between its nose radius of curvature and bluntness (equations (45) and (46)) at different clock angles. Fortunately, large Mach numbers are common for the solar wind at large heliocentric distances where Jupiter's and Saturn's obstacles have specific flattened shape.

[50] Since our bow shock model relied only on simple, geometrical characteristics of the obstacle, that is, position, radius of curvature (principal radii), and bluntness of its nose, it provides possibility of bow shock model utilization for a wide class of available magnetopause models (e.g., see Table A1) as well as for optional new, yet to be developed magnetopause models.

Appendix A: Obstacle Shape Parameterization

[51] Table A1 presents the summary of expressions usually used for the description of the nose part of the magnetopause during empirical analysis of observations. Interrelations between the first five expressions and relation (1) are quite straightforward because they are all conic sections. Interrelation between the expression by *Shue et al.* [2000] and relation (1) was obtained by their expansion into series in the vicinity of point $x = r_0$.

[52] For theoretical calculations of a flow around space obstacles, boundary conditions were frequently set up at the border of the obstacle shape of which was determined from the pressure balance equation [see, e.g., *Spreiter and Stahara*, 1992]:

$$k\rho V^2 \cos^2\psi + \{0, \text{or } p_0, \text{or } p_0 \sin^2\psi\} = p(r), \qquad \text{(A1)}$$

where ψ is the angle between V and normal to the obstacle boundary, p_0 stands for the thermal pressure in the upstream flow, $p(r)$ is the radial profile of the pressure inside the obstacle, and

$$k = \frac{1}{\gamma}\left(\frac{\gamma+1}{2}\right)^{(\gamma+1)/(\gamma-1)}\left(\gamma - \frac{\gamma-1}{2M_s^2}\right)^{1/(1-\gamma)}. \qquad \text{(A2)}$$

Table A1. Expressions Used in Space Science Papers for Magnetopause Shapes and Proper Nose Curvature Radii and Bluntnesses

Reference	Nose Part Equation	Interrelation With Equation (1)
Holzer and Slavin [1978]	$r = l/(1 + \varepsilon\cos\vartheta)$	$r_0 = l/(1 + \varepsilon)$, $R_0 = l$, $b_0 = \varepsilon^2 - 1$
Roelof and Sibeck [1993]	$y^2 + ax^2 + bx + c = 0$	$ar_0^2 + br_0 + c = 0$, $R_0 = ar_0 + b/2$, $b_0 = -a$
Petrinec and Russell [1996]	$r = r_0(1 + \varepsilon)/(1 + \varepsilon\cos\vartheta)$	$R_0 = r_0(1 + \varepsilon)$, $b_0 = \varepsilon^2 - 1$
Kawano et al. [1999], Parametric, ϑ - Parameter	$x = (r_0 - x_0)(1 + \varepsilon)\cos\vartheta/(1 + \varepsilon\cos\vartheta) + x_0$ $y = (r_0 - x_0)(1 + \varepsilon)\sin\vartheta/(1 + \varepsilon\cos\vartheta)$	$R_0 = (r_0 - x_0)(1 + \varepsilon)$, $b_0 = \varepsilon^2 - 1$
Kuznetsov and Yushkov [2000]	$x = r_0 - gy^2$	$R_0 = 1/(2g)$, $b_0 = 0$
Shue et al. [2000]	$r = r_0(2/(1 + \cos\vartheta))^{\alpha}$	$R_0 = 2r_0/(2-\alpha)$, $b_0 = (6\alpha - 8)(\alpha - 1)/(\alpha - 2)^3$
Spreiter et al. [1966]	equation (A1), $p_0 = 0$, $p(r) = p(r_0) \cdot (r_0/r)^6$	$R_0 = r_0\left(3 + \sqrt{21}\right)/6$, $b_0 = -\left(19 + \sqrt{21}\right)/30$
Spreiter et al. [1970]	equation (A1), $p_0 = 0$, $p(r) = p(r_0)\exp((r_0 - r)/H)$	$R_0 = r_0\left(1 + \sqrt{1 + 8H/r_0}\right)/2$, $b_0 = -1 + 2\,(1 + 2H/r_0)/(8 + R_0/H)$
Verigin et al. [1997]	equation (A1), $p_0 \neq 0$, $p(r) = p(r_0) \cdot [(1 - \xi)\,(r_0/r)^6 + \xi \cdot \exp((r_0 - r)/H)]$	$R_0 = \frac{r_0}{2}\left(1 + \sqrt{1 + \frac{8(1 - p_0/p(r_0))}{6(1-\xi) + \xi r_0/H}}\right)$, $b_0 = -1 + \dfrac{\frac{2(1-p_0/p(r_0))}{6(1-\xi)H/r_0 + \xi}\left(\frac{42(1-\xi)H^2/r_0^2 + \xi}{6(1-\xi)H/r_0 + \xi} + \frac{H}{r_0}\right) - 1}{4 + \frac{6(1-\xi)H/r_0 + \xi}{2(1-p_0/p(r_0))} \cdot \frac{R_0}{H}}$

Taking into account that $\cos^2\psi = 1/(1 + (dx/dy)^2)$, $\sin^2\psi = (dx/dy)^2/(1 + (dx/dy)^2)$, all three equation (A1) can be rewritten as

$$\frac{dx}{dy} = -\sqrt{\frac{p(r_0) - p_0}{p(r) - p_0} - 1}. \tag{A3}$$

Solution of the differential equation (A3) in the vicinity of $x = r_0$ is

$$x(y) \approx r_0 - \frac{y^2}{2R_0} + b_0\frac{y^4}{8R_0^3} - \ldots, \tag{A4}$$

where

$$R_0 = \frac{r_0}{2}\left(1 + \sqrt{1 - \frac{8(p(r_0) - p_0)}{r_0 p'(r_0)}}\right), \tag{A5}$$

$$b_0 = -1 + \frac{\dfrac{2(p(r_0) - p_0)}{p'(r_0)}\left(\dfrac{p''(r_0)}{p'(r_0)} - \dfrac{1}{r_0}\right) - 1}{4 - \dfrac{p'(r_0)R_0}{2(p(r_0) - p_0)}}. \tag{A6}$$

The general relations (A5) and (A6) provide the possibility to determine the nose radius of curvature R_0 and bluntness b_0 for the obstacles with spherically symmetric internal pressure profile $p(r)$. Specific cases of "dipole," "ionospheric," and "combined" obstacles are shown as lines 7–9 in Table A1, respectively.

Appendix B: Nonaxially Symmetric Curved Shock Boundary Condition

[53] In place of relation (31) the nonaxially symmetric shock surface equation F in the vicinity of its nose r_s can be expressed via its principal radii of curvature R_{sy}, R_{sz} as

$$F(x, y, z) = \frac{y^2}{2R_{sy}} + \frac{z^2}{2R_{sz}} - (r_s - x) = 0$$

or

$$F(x, \sigma, \varphi) = \frac{\sigma^2}{2R_{s\varphi}} - (r_s - x) = 0, \tag{B1}$$

where

$$\frac{1}{R_{s\varphi}} = \frac{\cos^2\varphi}{R_{sy}} + \frac{\sin^2\varphi}{R_{sz}} \tag{B2}$$

is the reciprocal radius of curvature of the shock nose in the plane φ = const. Figure B1a defines the Cartesian and cylindrical reference frames used in the above relations. The cross section of the bow shock by a plane x = const is an ellipsoid with square $S(x)$ (Figure B1b):

$$S = 2\pi\sqrt{R_{sy}R_{sz}}(r_s - x). \tag{B3}$$

The inner normal vector $\boldsymbol{n}$ to the shock surface at the border of this ellipsoid can be expressed as

$$\begin{aligned}\boldsymbol{n} &= -\frac{\nabla F}{|\nabla F|} = (n_x, n_\sigma, n_\varphi) \\ &\approx \left(-1, -\sqrt{\frac{2(r_s - x)}{R_{s\varphi}}}, \sqrt{2R_{s\varphi}(r_s - x)}\sin\varphi\cos\varphi\left(\frac{1}{R_{sy}} - \frac{1}{R_{sz}}\right)\right).\end{aligned} \tag{B4}$$

The application of the Rankine-Hugoniot relations (equation (10)) to the normal and tangential components of the upstream velocity vector $\boldsymbol{V} = (-V, 0, 0)$ provides the possibility to evaluate the postshock velocity $\boldsymbol{V}_1$ as

$$\begin{aligned}\boldsymbol{V}_1 = (V_{1x}, V_{1\sigma}, V_{1\varphi}) \approx V\Bigg(&-\varepsilon, (1 - \varepsilon)\sqrt{\frac{2(r_s - x)}{R_{s\varphi}}}, \\ &-(1 - \varepsilon)\sqrt{2R_{s\varphi}(r_s - x)}\sin\varphi\cos\varphi\left(\frac{1}{R_{sy}} - \frac{1}{R_{sz}}\right)\Bigg).\end{aligned} \tag{B5}$$

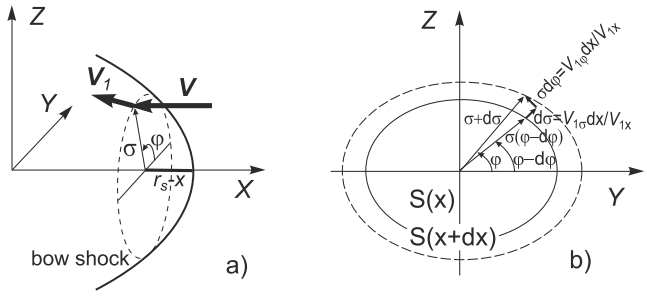

Figure B1. (a) Definition of the used reference frames and (b) main geometric relations relevant to calculation of the rate of increase of the flow tube cross section $S(x)$.

All terms of the order of $(r_s - x)$ or less were omitted in equations (B4) and (B5). During time dt after passing of the shock at the border of ellipsoid $S(x)$ at clock angle $\varphi - d\varphi$ (Figure B1b), a parcel of gas will be displaced from $r_s - x$ by $dx = V_{1x}dt = -\varepsilon V dt$ along the x axis, from $\sigma(\varphi - d\varphi)$ by $d\sigma = V_{1\sigma}dt = V_{1\sigma}/V_{1x}dx$ along the σ axis, and from $\varphi - d\varphi$ by $d\varphi = V_{1\varphi}/\sigma dt = V_{1\varphi}/V_{1x}dx/\sigma$ along the φ axis. So, the new radial distance at φ clock angle will be $(\sigma + d\sigma)|_\varphi = \sigma(\varphi - d\varphi) + V_{1\sigma}/V_{1x}dx = \sigma(\varphi) - \dot{\sigma}d\varphi + V_{1\sigma}/V_{1x}dx = \sigma(\varphi) - \dot{\sigma}/\sigma V_{1\varphi}/V_{1x}dx + V_{1\sigma}/V_{1x}dx = \sigma(\varphi) + (V_{1\sigma} - \dot{R}_{s\varphi}/R_{s\varphi}V_{1\varphi}/2)/V_{1x}dx$, where $\dot{}$ marks differentiation over φ. That is, the rate of expansion of the radial distance of the original flow tube $S(x)$ at clock angle φ can be expressed as

$$\frac{d\sigma}{dx} = \frac{1}{V_{1x}}\left(V_{1\sigma} - \frac{\dot{R}_{s\varphi}}{2R_{s\varphi}}V_{1\varphi}\right) = -\frac{1-\varepsilon}{\varepsilon}\sqrt{\frac{2(r_s - x)}{R_{s\varphi}}}\left(1 + R_{s\varphi}^2 \sin^2\varphi\cos^2\varphi\left(\frac{1}{R_{sy}} - \frac{1}{R_{sz}}\right)^2\right). \quad \text{(B6)}$$

The last equality in equation (B6) is the result of the substitutions of relations (B2) and (B5).

[54] Taking into account relations (B1), (B2), and (B6), the relative rate of the flow tube expansion after the curved shock can be written as

$$\frac{1}{S}\frac{dS}{dx} = \frac{1}{S}\int_0^{2\pi}\sigma\frac{d\sigma}{dx}d\varphi = -\frac{1-\varepsilon}{\varepsilon}\frac{2}{\sqrt{R_{sy}R_{sz}}} \cdot\left(1 + \frac{(R_{sy} - R_{sz})^2}{2\pi}\int_0^{2\pi}\frac{\sin^2\varphi\cos^2\varphi d\varphi}{(R_{sy}\sin^2\varphi + R_{sz}\cos^2\varphi)^2}\right). \quad \text{(B7)}$$

Completing the integration in equation (B7) leads to the final shape of the nonaxially symmetric curved shock boundary condition:

$$\frac{1}{S}\frac{dS}{dx} = -\frac{2}{\langle R_s\rangle}\cdot\frac{1-\varepsilon}{\varepsilon}. \quad \text{(B8)}$$

Boundary condition (B8) looks similar to that of equation (13) for axially symmetric shocks, but the average radius of curvature $\langle R_s\rangle$ replaces R_s with

$$\frac{1}{\langle R_s\rangle} = \frac{1}{2}\left(\frac{1}{R_{sy}} + \frac{1}{R_{sz}}\right). \quad \text{(B9)}$$

[55] **Acknowledgments.** This work was performed while one of the authors (M. V.) held a NRC Associateship Award at NASA/GSFC, partially supported by OTKA grant T037844 of the Hungarian Science Fund, and by the Canadian Space Agency (KK). Space Research Institute authors would like to thank M. G. Lebedev and V. P. Stulov for useful discussions.

[56] Shadia Rifai Habbal thanks K. Schwingenschuh and another reviewer for their assistance in evaluating this paper.

References

Ambrosio, A., and A. Wortman, Stagnation-point shock-detachment distance for flow around spheres and cylinders in air, *J. Aerospace Sci.*, *29*(7), 875, 1962.

Biermann, L., B. Brosowski, and H. U. Schmidt, The interaction of the solar wind with a comet, *Solar Phys.*, *1*, 254–284, 1967.

Fairfield, D. H., I. H. Cairns, M. D. Desch, A. Szabo, A. J. Lazarus, and M. R. Aellig, The location of low Mach number bow shocks at Earth, *J. Geophys. Res.*, *106*, 25,361–25,376, 2001.

Farris, M. H., and C. T. Russell, Determining the standoff distance of the bow shock: Mach number dependence and use of the models, *J. Geophys. Res.*, *99*, 17,681–17,689, 1994.

Farris, M. H., S. M. Petrinec, and C. T. Russell, The thickness of the magnetosheath: Constraints on the polytropic index, *Geophys. Res. Lett.*, *18*(10), 1821–1824, 1991.

Hayes, W. D., and R. F. Probstein, *Hypersonic Flow Theory, Inviscid Flow*, vol. 1, Academic, San Diego, Calif., 1966.

Hida, K., Asymptotic behavior of the location of a detached shock wave in a nearly sonic flow, *J. Phys. Soc. Japan*, *10*(10), 882–889, 1955.

Holzer, R. E., and J. A. Slavin, Magnetic flux transfer associated with expansion and contraction of the dayside magnetosphere, *J. Geophys. Res.*, *83*, 3831–3839, 1978.

Kawano, H., S. M. Petrinec, C. T. Russell, and T. Higuchi, Magnetopause shape determination from measured position and estimated flaring angle, *J. Geophys. Res.*, *104*, 247–261, 1999.

Kuznetsov, S. N., and B. Y. Yushkov, Magnetopause position dependence on the interplanetary magnetic field B_z-component: Analysis of the pressure balance equation, *Phys. Chem. Earth, Part C*, *25*(1–2), 165–168, 2000.

Landau, L. D., and E. M. Lifshitz, *Fluid Mechanics*, Pergamon, New York, 1959.

Lyubimov, A. N., and V. V. Rusanov, *Gas Flows Around Blunt Bodies,* vol. 1, *Methods of Calculations and Flows Analysis,* vol. 2, *Tables of Gasdynamic Parameters* (in Russian), Nauka, Moscow, 1970.

Lyubimov, A. N., N. M. Tyumnev, and G. I. Hut, *Methods of the Studies of the Gas Flow and of Determination of Aerodynamic Properties of Axially Symmetric* Bodies (in Russian)Nauka, Moscow, 1995.

Maslennikov, V. G., On the shape of the detached shock wave formed by supersonic motion of hemisphere and cylinder in different gases, in *Aerophysical Studies of Supersonic Flows*, pp. 256–264, Nauka, Moscow, 1967.

Minailos, A. N., Similarity parameters and approximating relations for axially symmetric flow past ellipsoids, *Fluid Dyn.*, *8*, 494–498, 1973.

Petrinec, S. M., and C. T. Russell, Near-Earth magnetotail shape and size as determined from the magnetopause flaring angle, *J. Geophys. Res.*, *101*, 137–152, 1996.

Roelof, E. C., and D. G. Sibeck, Magnetopause shape as a bivariate function of interplanetary magnetic field B_z and solar wind dynamic pressure, *J. Geophys. Res.*, *98*, 21,421–21,450, 1993.

Seiff, A., Recent information on hypersonic flow fields, in *Gas Dynamics in Space Explorations, NASA Spec. Publ. SP-24*, 19–32, 1962.

Serbin, H., Supersonic flow around blunt bodies, *J. Aeronaut. Sci.*, *25*(1), 58–59, 1958.

Shue, J.-H., P. Song, C. T. Russell, J. K. Chao, and Y.-H. Yang, Toward predicting the position of the magnetopause within geosynchronous orbit, *J. Geophys. Res.*, *105*, 2641–2656, 2000.

Shugaev, F. V., Axially symmetric flow far of the obstacle in the vicinity of the axis when M_∞ number approaching to unit (in Russian), *Appl. Math. Mech.*, *28*(1), 184–185, 1964.

Shugaev, F. V., Interaction of the supersonic flow with blunt bodies (in Russian), Ph. D thesis, Moscow State Univ., Moscow, 1965.

Slavin, J. A., and R. E. Holzer, Solar wind flow about the terrestrial planets: 1. Modeling bow shock position and shape, *J. Geophys. Res.*, *86*, 11,401–11,418, 1981.

Slavin, J. A., R. E. Holzer, J. R. Spreiter, S. S. Stahara, and D. S. Chaussee, Solar wind flow about the terrestrial planets: 2. Comparisons with gasdynamic theory and implications for solar-planetary interactions, *J. Geophys. Res.*, *88*, 19–35, 1983.

Slavin, J. A., E. J. Smith, J. R. Spreiter, and S. S. Stahara, Gasdynamic modeling of the Jupiter and Saturn bow shocks: Solar wind flow about the outer planets, *J. Geophys. Res.*, *90*, 6275–6286, 1985.

Song, P., C. T. Russell, T. I. Gombosi, J. R. Spreiter, S. S. Stahara, and X. X. Zhang, On the processes in the terrestrial magnetosheath, 1, Scheme development, *J. Geophys. Res.*, *104*, 22,345–22,355, 1999.

Spreiter, J. R., and S. S. Stahara, A new predictive model for determining solar wind terrestrial planet interaction, *J. Geophys. Res.*, *85*, 6769–6777, 1980.

Spreiter, J. R., and S. S. Stahara, Computer modeling of solar wind interactions with Venus and Mars, in *Venus and Mars: Atmospheres, Ionospheres and Solar Wind Interactions*, *Geophys. Monogr. Ser.*, vol. 66, edited by J. H. Luhmann, M. Tatrallyay, and R. O. Repin, pp. 345–383, AGU, Washington D. C., 1992.

Spreiter, J. R., and S. S. Stahara, Magnetohydrodynamic and gasdynamic theories for planetary bow waves, in *Collisionless Shocks in the Heliosphere: Reviews of Current Research*, *Geophys. Monogr. Ser.*, vol. 35, edited by B. T. Tsurutani and R. G. Stone, pp. 85–107, AGU, Washington, D. C., 1985.

Spreiter, J. R., and S. S. Stahara, The location of the planetary bow shocks: A critical overview of theory and observations, *Adv. Space. Res.*, *15*(8/9), 433, 1995.

Spreiter, J. R., A. L. Summers, and A. W. Rizzi, Solar wind flow past nonmagnetic planets-Venus and Mars, *Planet. Space Sci.*, *18*, 1281–1299, 1970.

Spreiter, J. R., A. L. Summers, and A. Y. Alksne, Hydromagnetic flow around the magnetosphere, *Planet. Space Sci.*, *14*, 223–253, 1966.

Stahara, S. S., R. R. Rachiele, J. R. Spreiter, and J. A. Slavin, A 3-dimensional gasdynamic model for solar-wind flow past nonaxisymmetric magnetospheres: Application to Jupiter and Saturn, *J. Geophys. Res.*, *94*, 13,353–13,365, 1989.

Stulov, P. V., Similarity law for supersonic flow past blunt bodies, *Fluid Dyn.*, *4*, 93–96, 1969.

Van Dyke, M. D., The supersonic blunt-body problem-Review and extension, *J. Aerosp. Sci.*, *25*(8), 485–496, 1958.

Verigin, M., et al., Quantitative model of the Martian magnetopause shape and its variation with the solar wind ram pressure based on Phobos 2 observations, *J. Geophys. Res.*, *102*, 2147–2155, 1997.

Verigin, M. I., et al., Studies of the Martian bow shock response to the variation of the magnetosphere dimensions according to TAUS and MAGMA measurements aboard the PHOBOS 2 orbiter, *Adv. Space Res.*, *20*(2), 155–158, 1997a.

Verigin, M. I., et al., Shape and location of planetary bow shocks, *Cosmic Res.*, *37*(1), 34–39, 1999.

Verigin, M. I., et al., Analysis of the 3-D shape of the terrestrial bow shock by Interball/Magion 4 observations, *Adv. Space Res.*, *28*(6), 857–862, 2001a.

Verigin, M., G. Kotova, A. Szabo, J. Slavin, T. Gombosi, K. Kabin, F. Shugaev, and A. Kalinchenko, Wind observations of the terrestrial bow shock: 3-D shape and motion, *Earth Planets Space*, *53*(10), 1001–1009, 2001b.

Wallis, M. K., Weakly-shocked flows of the solar wind plasma through atmospheres of comets and planets, *Planet. Space Sci.*, *21*, 1647–1660, 1973.

T. Gombosi, Space Physics Research Laboratory, Department of Atmospheric, Oceanic and Space Sciences, University of Michigan, 2455 Hayward Street, Ann Arbor, MI 48109-2143, USA. (tamas@umich.edu)

K. Kabin, Department of Physics, University of Alberta, Edmonton, Alberta, Canada T6G 2J1. (Kabin: kabin@phys.ualberta.ca)

G. Kotova, O. Plochova, and M. Verigin, Space Research Institute, Russian Academy of Sciences, Profsoyuznaya, 84/32, Moscow 117997, Russia. (kotova@iki.rssi.ru; plochova@iki.rssi.ru; verigin@iki.rssi.ru)

F. Shugaev, Physical Faculty, Moscow State University, Moscow 119899, Russia. (shugaev@phys.msu.su)

J. Slavin and A. Szabo, NASA Goddard Space Flight Center, Code 696, Greenbelt, MD 20771, USA. (james.a.slavin@gsfc.nasa.gov; Adam.Szabo@gsfc.nasa.gov)

K. Szegö and M. Tátrallyay, KFKI Research Institute for Particle and Nuclear Physics, P. O. Box 49, H-1525 Budapest, Hungary. (szego@rmki.kfki.hu; mariella@rmki.kfki.hu)